

Thermal Transport in Multidimensional Silicon-Graphene Hybrid Nanostructures

Wei Gong,⁺ Raghav Garg,⁺ Ruiqiang Guo,⁺ Sangyeop Lee,^{*} Tzahi Cohen-Karni,^{*} and Sheng Shen^{*}Cite This: *ACS Appl. Mater. Interfaces* 2021, 13, 50206–50212

Read Online

ACCESS |



Metrics & More



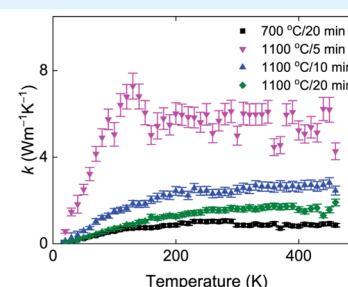
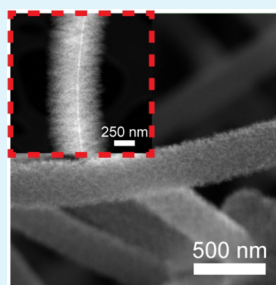
Article Recommendations



Supporting Information

ABSTRACT: In this work, we fabricate multidimensional silicon-graphene hybrid nanostructures composed of three-dimensional (3D) out-of-plane graphene flakes on a silicon nanowire core. By changing the synthesis temperature (700 and 1100 °C) and time (5, 10, and 20 min), we obtain two different types of 3D graphene flakes with tunable dimensions and structure parameters. We characterize the thermal transport behavior of this hybrid multidimensional material in a broad temperature range of 20–460 K. With different morphologies and structures, the effective thermal conductivity of the silicon-graphene hybrid nanostructures varies from 1 to 7 W/(m·K) at room temperature. We also apply molecular dynamics simulation and density functional theory to elucidate the thermal transport mechanisms in the silicon-graphene hybrid nanostructures.

KEYWORDS: multidimensional silicon-graphene hybrid nanowires, 3D graphene flakes, thermal conductivity



INTRODUCTION

Since Novoselov et al. successfully obtained graphene using mechanical exfoliation in 2004,¹ research on graphene has tremendously increased. As the most famous two-dimensional (2D) material, graphene has been widely studied on its fabrication, characterization, and application.^{2–6} The thermal conductivity of the large-size, defect-free, single-layer graphene can reach as high as 3000–5000 W/(m·K),^{7,8} which is the highest among all existing materials. Yet, most of the research on graphene is mainly based on its 2D morphology. Recently, we successfully synthesized fuzzy graphene, a complex out-of-plane three-dimensional (3D) graphene flake structure grown on the surface of silicon nanowire templates⁹ using a plasma-enhanced chemical vapor deposition (PECVD) method. The measured electrical properties contributed by the fuzzy graphene structures are distinct from 2D graphene and bulk graphite or amorphous carbon,¹⁰ indicating the unique properties of this new complex multidimensional structure built by 3D graphene flakes. However, the thermal transport properties of the new hybrid structures remain unknown. In this work, we measure the thermal transport properties of multidimensional silicon-graphene hybrid nanostructures composed of 3D fuzzy graphene flakes on a silicon nanowire core (3DFG-Si NW) in a wide temperature range of 20–460 K. By modulating the synthesis conditions, we manipulate the resulting 3D structures of the graphene flakes and tune the thermal transport performance. We employ simulation methods based on density functional theory (DFT) and molecular dynamics (MD) to elucidate the nanoscale thermal

transport mechanisms in 3DFG-Si NWs. Combining the measurement and simulation results, we also establish a connection between the structure and the thermal transport properties.

The hybrid, multidimensional 3DFG-Si NWs are obtained via a two-step synthesis process (see the [Materials and Methods](#) section).^{9,10} The intrinsic silicon nanowires (i-SiNWs) as the core are synthesized following a Au nanoparticle (AuNP) catalyzed vapor–liquid–solid (VLS) process.¹¹ Out-of-plane graphene flakes are grown directly on the SiNW template following PECVD.⁹ We have previously reported that altering the synthesis conditions, i.e., temperature, partial pressure of the CH₄ precursor, and synthesis duration, enables tight control over the overall geometry and arrangement of 3DFG-Si NWs.^{9,10,12} Specifically, in this work, we tune the density and size of the free-standing graphene flakes by varying the synthesis temperature and time¹³ and focus on their influence on the thermal transport properties of 3DFG-Si NWs.

Received: May 1, 2021

Accepted: October 8, 2021

Published: October 18, 2021



RESULTS AND DISCUSSION

To synthesize 3DFG-Si NWs with different densities and sizes of free-standing graphene flakes, we vary the synthesis temperature between 700 and 1100 °C and the synthesis duration from 5 to 20 min. An increase in the diameter of 3DFG-Si NWs from 212 ± 14 to 644 ± 42 nm is observed as the synthesis temperature is increased from 700 to 1100 °C both for 20 min, respectively (Figure 1a,d). Regulating the

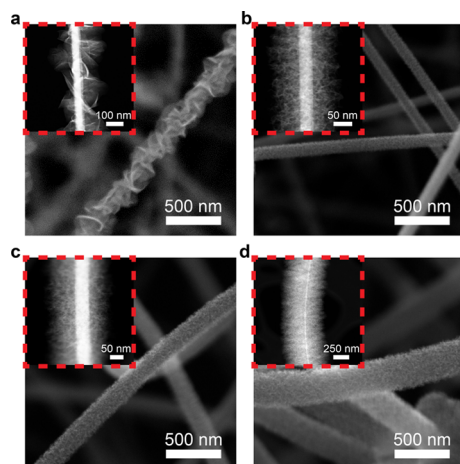


Figure 1. Structure of 3DFG-Si NWs. Representative scanning electron microscopy (SEM) images of 3DFG-Si NWs synthesized at (a) 700 °C for 20 min, (b) 1100 °C for 5 min, (c) 1100 °C for 10 min, and (d) 1100 °C for 20 min. Insets are representative scanning transmission electron microscopy (STEM) images of 3DFG-Si NWs synthesized at the respective conditions.

synthesis time from 5 to 10 and 20 min at a constant synthesis temperature of 1100 °C results in 3DFG-Si NWs increasing from 134 ± 7 to 231 ± 15 and 644 ± 42 nm, respectively (Figure 1b–d). We also observe a density increase in the free-standing graphene flakes as the synthesis temperature is increased. As a comparison, increasing the temperature from 700 to 1100 °C while decreasing the duration from 20 to 10 min allows us to attain 3DFG-Si NWs with higher graphene flake density but similar 3DFG-Si NW diameters (Figure 1a,c). At 1100 °C, increasing the synthesis time leads to the density increase in free-standing graphene flakes (Figure 1b–d).

The high-resolution transmission electron microscopy (HRTEM) characterization results demonstrate that the 700 °C 3DFG-Si NW has a drastically different structure as compared to the 1100 °C 3DFG-Si NW. Individually free-standing graphene flakes are easily identified for the 3DFG-Si NW synthesized at 700 °C, while the density of graphene flakes increases for the 3DFG-Si NW synthesized at 1100 °C (Figure 2a,d). The increased density of graphene flakes leads to an increase in inter-flake contacts and junctions for the 3DFG-Si NW synthesized at 1100 °C. A graphitic shell is identified to conformally coat the 3DFG-Si NW synthesized at 700 °C (marked white lines; Figure 2a,b). Due to the high density of free-standing graphene flakes, the presence of such a graphitic shell around the SiNW core is not clearly identified through HRTEM imaging for the 3DFG-Si NW synthesized at 1100 °C (Figure 2e). It should be noted that 3DFG-Si NWs have a polycrystalline network of single-to-few layer graphene (Figure 2c,f and see Supporting Information for details on Raman spectroscopy).

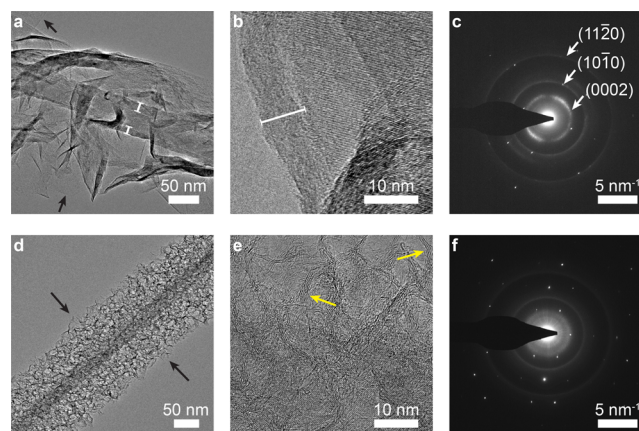


Figure 2. HRTEM characterization of 3DFG-Si NWs. (a) Representative HRTEM image, (b) zoomed-in HRTEM image, and (c) selected area electron diffraction (SAED) of 3DFG-Si NWs synthesized at 700 °C for 20 min. (d) Representative HRTEM image, (e) zoomed-in HRTEM image, and (f) SAED of 3DFG-Si NWs synthesized at 1100 °C for 10 min. Black and yellow arrows denote single- and multilayer free-standing graphene flakes, respectively. Marked white lines denote the graphitic shell around the i-SiNW core.

We investigate the structure of the free-standing graphene flakes by performing electron energy loss spectroscopy (EELS) across a number of points along the thickness of individual 3DFG-Si NWs synthesized under different synthesis conditions (Figure 3a,c,e,g). From the EELS data of the carbon K-edge regions acquired for all 3DFG-Si NWs, we observe a sharp peak at 285.5 eV and a broad peak between 290 and 310 eV, which are due to the transition from $1s$ to π^* states and the transition from $1s$ to σ^* states (Figure 3b,d,f,h),^{10,14,15} respectively. These transitions confirm the sp^2 structure of the graphene lattice in 3DFG-Si NWs.¹⁶ Multiple scattering events lead to oscillations that can be identified by the emergence of interference peaks at ~ 320 eV.^{10,17} The intensity of these interference peaks can be used to distinguish between graphitic and graphene-like structures in 3DFG-Si NWs. We do not observe the presence of strong interference peaks in the spectra acquired from the edge regions of all 3DFG-Si NWs (Figure 3b,d,f,h). In the case of 3DFG-Si NWs synthesized at 700 °C for 20 min, we observe an increase in the intensity of the interference peaks at positions closer to the SiNW core (Figure 3a). This suggests that 3DFG-Si NWs synthesized at 700 °C for 20 min primarily consist of free-standing single-layer graphene with a thin graphitic shell closer to the SiNW core.^{15,18,19} This is corroborated by the presence of a thin shell surrounding the SiNW core as observed in the corresponding STEM and TEM images (Figures 1a, 2a–c, and 3a). Increasing the synthesis temperature to 1100 °C increases the thickness of the graphitic shell, as observed by the increasing intensity of the interference peaks closer to the radial edge of the 3DFG-Si NW (Figure 3c–h). Increased scattering events due to the high density of graphene flakes in the case of the 3DFG-Si NW synthesized at 1100 °C for 20 min can be attributed to the increased intensity of the interference peaks.

To understand the fundamental thermal transport in 3DFG-Si NWs, we measure the thermal transport properties of 3DFG-Si NWs using a micro thermal device with two suspended islands (Figure 4a).²⁰ To measure the thermal conductivity and thermal conductance of 3DFG-Si NWs, we use a DC current to heat up the heating island and apply an

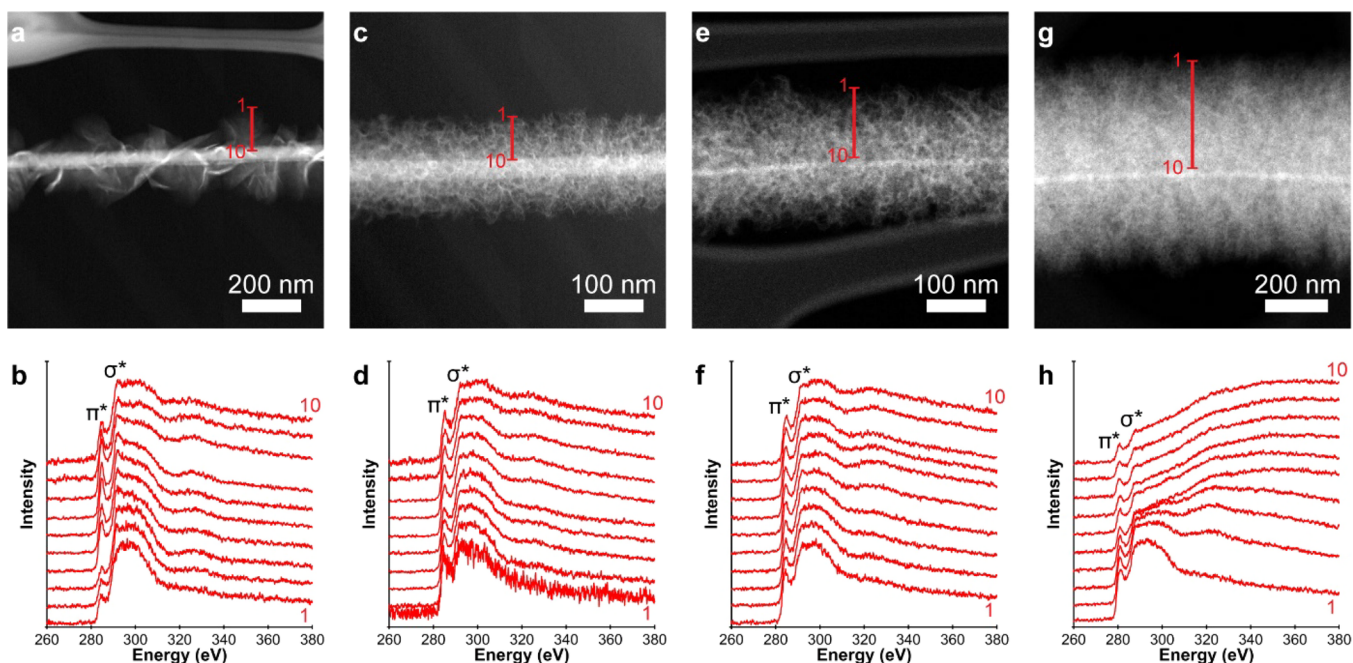


Figure 3. EELS characterization of isolated 3DFG-Si NWs. (a) STEM image and (b) EELS line scan from points along the marked line in panel (a) of 3DFG-Si NWs synthesized at 700 °C for 20 min. (c) STEM image and (d) EELS line scan from points along the marked line in panel (c) of 3DFG-Si NWs synthesized at 1100 °C for 5 min. (e) STEM image and (f) EELS line scan from points along the marked line in panel (e) of 3DFG-Si NWs synthesized at 1100 °C for 10 min. (g) STEM image and (h) EELS line scan from points along the marked line in panel (g) of 3DFG-Si NWs synthesized at 1100 °C for 20 min.

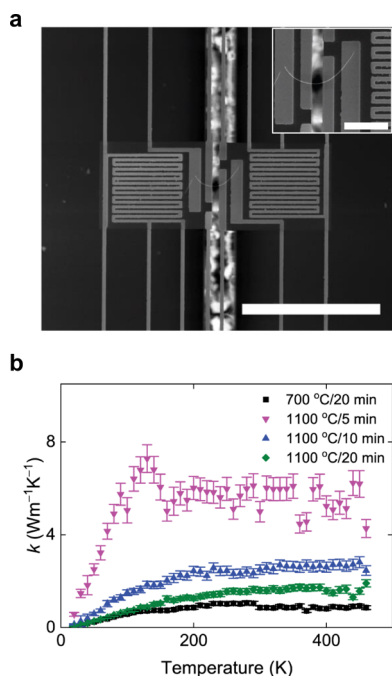


Figure 4. Thermal property characterization of 3DFG-Si NWs. (a) SEM image of one 3DFG-Si NW on the micro thermal device. Scale bar: 50 μm . Inset: Zoomed-in image. Scale bar: 10 μm . (b) Thermal conductivity k of 3DFG-Si NWs as a function of temperature, in which each dataset has the number of independent replicates ($n = 2$), and the error bar of each measurement point is calculated based on >50 data points.

AC current to both the islands of the micro thermal device. In all the measurements, we increase the DC current from 0 to 20 μA with a step of $\sim 0.2 \mu\text{A}$, in which the experimental data are

collected after thermal equilibrium is reached for the whole device. Electron or ion beam-assisted Pt/C contacts are conventionally deposited at the nanowire-device contact pads to reduce the contact resistance. However, in the case of 3DFG-Si NWs, the deposition of Pt contacts by focused ion beam causes unwanted structural changes in the graphene flakes (see the Supporting Information, Figure S2). Instead, we directly bridge the two islands using a 3DFG-Si NW and mechanically make contacts between the 3DFG-Si NW and the micro device. The thermal contact resistance is calibrated by measuring the thermal conductance of samples with different lengths. The results show that the thermal contact resistance counts about 5% of the total resistance and thus can be neglected (see the Supporting Information).

As a reference, we first measure the thermal conductivity of a SiNW from 20 to 460 K, which agrees well with previous results in the literature²¹ (see the Supporting Information). The effective thermal conductivity measurement results for 3DFG-Si NWs are shown in Figure 4b, where the thermal conductivity k is calculated based on the measured thermal conductance of 3DFG-Si NWs using the micro thermal devices and the geometries measured by TEM. At room temperature, the 1100 °C/5 min sample has the highest thermal conductivity of up to $\sim 6 \text{ W}/(\text{m}\cdot\text{K})$. We observe that, as the synthesis times of 3DFG-Si NWs increase to 10 and 20 min at 1100 °C, the thermal conductivities decrease to ~ 2 and $\sim 1 \text{ W}/(\text{m}\cdot\text{K})$, respectively. Compared with the 3DFG-Si NWs synthesized at 1100 °C, the 3DFG-Si NW synthesized at 700 °C for 20 min exhibits the lowest thermal conductivity of $\sim 0.8 \text{ W}/(\text{m}\cdot\text{K})$ at room temperature because the graphene flakes are distributed sparsely along the radial direction with few flake-flake junctions. The uncertainty in the thermal conductivity measurements is determined for individual devices (see the Supporting Information), which are representative of the entire

population of 3DFG-Si NWs synthesized under a particular condition. Each dataset in Figure 4b is for one individual 3DFG-Si NW sample, where the error bar of each measurement point is calculated based on >50 data points acquired by varying the applied DC current on the micro thermal device. For each dataset, the value and trend are representative and repeatable for at least two samples under the same synthesis conditions.

Based on the measured thermal conductivity of the SiNW core, we also extract the thermal conductivity of the 3D graphene layers k_{GL} of 3DFG-Si NWs. To extract k_{GL} from the measured thermal conductivity, we use the parallel thermal resistance model assuming that the SiNW core has the same thermal conductivity for all samples. The parallel resistance model is suitable for our 3DFG-Si NWs considering the weak van der Waals interaction between the core and the graphene flakes. The model has also been used for core-shell nanowires and nanocomposites where the interactions between the core and shell/matrix are similarly weak.^{22–24} In Figure 5a, we

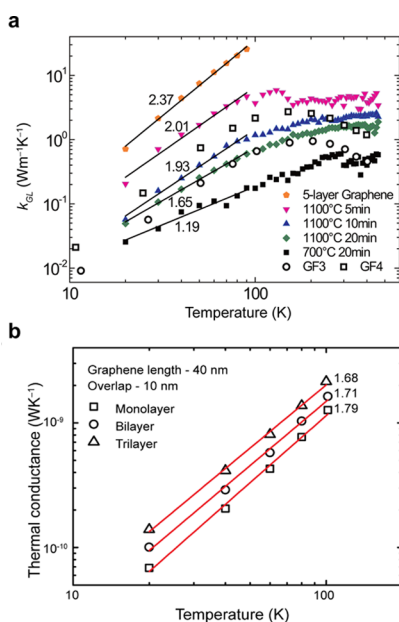


Figure 5. Temperature dependence of thermal conductivity values from the experiments and simulations. (a) Thermal conductivity of 3DFG-Si NWs synthesized under different conditions in comparison with graphene foams (GF3 and GF4 in ref 25) and the five-layer pristine graphene from DFT under the ballistic limit. The pristine graphene is assumed to have a sample size of 20 nm. The solid lines are fitting with T^α with the values of α . (b) Temperature dependence of the thermal conductance of graphene-graphene junctions for different numbers of graphene layers from MD simulations. The graphene flakes are assumed to have a length of 40 nm and overlap length of 10 nm with each other. The solid lines represent the T^α fit below 100 K, with the magnitude of α labeled.

compare the k_{GL} of 3DFG-Si NWs synthesized at 700 and 1100 °C as well as the previously reported graphene foam.²⁵ The k_{GL} of the 700 °C 3DFG-Si NWs includes the contribution of both the densely wrapped multiple layers of graphene and the dilute graphene flakes. Compared with the 1100 °C samples, the 700 °C 3DFG-Si NWs have a much lower k_{GL} . This can be attributed to the substantially low density of graphene flakes in the 700 °C sample. Because of the sparse distribution of graphene flakes along the radial direction,

many of them cannot form effective junctions, seriously preventing the heat flow. While the graphene foams show thermal conductivity increasing at low temperature and decreasing above a certain temperature, the k_{GL} of 3DFG-Si NWs synthesized at 1100 °C exhibits the plateau of thermal conductivity above a certain threshold temperature, which is a typical behavior of highly disordered materials. As the synthesis time increases, the threshold temperature increases from 130 K (5 min) to about 300 K (10 and 20 min) at 1100 °C. This behavior indicates enhanced phonon scattering in the graphene shells with the increased synthesis time.

We analyze how the synthesis time affects the thermal transport and its mechanisms using the temperature dependence of thermal conductivity. The k_{GL} below 100 K is fitted to T^α in Figure 5a. We find that the value of α decreases as the synthesis time increases. The value of α decreases from 2.01 for a synthesis duration of 5 min to 1.65 for a synthesis duration of 20 min. To understand the temperature dependence of k_{GL} and the threshold temperature in the graphene shells grown with different synthesis times, we consider two thermal transport mechanisms: the thermal conductance of graphene flakes without internal phonon scattering and the thermal conductance across junctions between them. Considering the size (20 ± 12 nm) of the graphene flakes that is much smaller than the mean free path of pristine graphene, it is reasonable to assume very weak internal phonon scattering and ballistic thermal transport within each graphene flake. Using atomistic simulations, we evaluate the temperature dependence of the two different mechanisms of thermal transport. The ballistic thermal conductance within each graphene flake is directly calculated with the phonon dispersion from the DFT calculation. The thermal conductance across junctions is studied using the non-equilibrium MD simulation of graphene flakes that have overlaps (see details in the Supporting Information). As shown in Figure 5a, the ballistic thermal conductivity of pristine five-layer graphene has a much stronger temperature dependence ($\alpha = 2.37$) than the measured results (for example, $\alpha = 2.01$ for the 5 min sample). In contrast, the junctions exhibit much weaker temperature dependence of thermal conductance. As shown in Figure 5b, its α value is ~ 1.7 and insensitive to the layer number, junction overlap length, and length of graphene (Figure S8 in the Supporting Information). Therefore, as the thermal transport across junctions becomes more important for thermal resistance, the overall thermal conductivity has less temperature dependence. These calculations explain the different temperature dependences of thermal conductivity of samples synthesized for varying time. The sample synthesized for 5 min in Figure 5a has a temperature dependence ($\alpha = 2.01$), which is between those of ballistic conductance and junctions. This can indicate that both flakes and junctions play important roles in thermal resistance. However, for the samples that are synthesized with longer time, the dependences of thermal conductivity on temperature are reduced to 1.93 for 10 min and 1.65 for 20 min, which are close to the behavior of junctions. This shows that the contribution of junctions to thermal resistance becomes larger as the synthesis time increases. The decreasing trend of the value of α is consistent with the experimental observation that the density of graphene flakes increases, and more junctions form with the synthesis time.

CONCLUSIONS

In this work, we fabricate multidimensional hybrid 3DFG-Si NWs by varying synthesis temperature and time. By changing the synthesis temperature from 700 to 1100 °C, we observe significant structure changes of 3DFG-Si NWs. The structure of the 700 °C 3DFG-Si NWs can be classified to a silicon core, a dense graphitic layer, and a sparse radially distributed graphene flake layer, while the structure of 1100 °C 3DFG-Si NWs can be viewed as a combination of the silicon core and the mesh-like porous graphene flake layer. We measure the thermal conductivity of 3DFG-Si NWs in a broad temperature range from 20 to 460 K and compare with the predictions based on the MD and DFT simulations. We identify the influence of both graphene flake density and flake–flake junction density on the thermal transport in 3DFG-Si NWs. Overall, the effective thermal conductivity of the graphene flakes in 3DFG-Si NWs can be as high as 1 W/(m·K), which is comparable with that of amorphous carbon and much larger than those of existing aerogel-like materials (typically in the range of 0.01–0.05 W/(m·K)²⁶), thus showing great potential for thermal management of micro- and nanoelectronics.

MATERIALS AND METHODS

SiNW Synthesis. SiNWs were synthesized using the AuNP-catalyzed VLS process, as described in our previous works.^{9,10,12} A 2.0 cm × 2.0 cm (100) Si substrate with a 600 nm thermal oxide (p-type, ≤0.005 Ω cm) was washed with acetone and isopropyl alcohol (IPA) in an ultrasonic bath for 5 min each, blow-dried with N₂, and further cleaned in a UV ozone system at 150 °C for 10 min. The substrates were functionalized first with 500 μL of 4:1 deionized (DI) water:poly-L-lysine (PLL) (0.1% w/v, Sigma-Aldrich) and then by 500 μL of 9:1 DI water:30 nm AuNP solution (Ted Pella). AuNP-coated substrates were introduced into a custom-built CVD setup. SiNW nucleation and synthesis were conducted at 450 °C under 20 sccm SiH₄ (10% in H₂, Matheson Gas) and 80 sccm H₂ (Matheson Gas) at 40 Torr. The sample was finally cooled to room temperature at base pressure.

3DFG-Si NW Synthesis. 3DFG was synthesized through the PECVD process following our previously described protocol.^{9,10,12} After the SiNW synthesis, the sample was immediately introduced to a custom-built PECVD setup. The synthesis was carried out at varying synthesis temperatures (700 and 1100 °C) and at a total pressure of 0.5 Torr. The temperature of the furnace was increased to the synthesis temperature at a rate of 55 °C per min under 100 sccm Ar (Matheson Gas). After inductively coupled plasma (ICP) was generated using a 13.56 MHz RF power supply with a constant plasma power of 50 W, the synthesis was conducted under a 50 sccm CH₄ precursor (5% CH₄ in Ar, Airgas) for varying synthesis times. Finally, the plasma was turned off and the sample was cooled to room temperature in 30 min under 100 sccm Ar flow.

Raman Spectroscopy. NT-MDT NTEGRA spectra with 532 and 633 nm excitations through a 100× objective were used for single- and dual-laser Raman analysis, respectively. A Si/600 nm SiO₂ chip was gently rubbed over a 3DFG-Si NW sample, and optical images of the Si/600 nm SiO₂ chip were acquired to identify individual nanowires. The Raman spectra from individual 3DFG-Si NW nanowires were then acquired with a 0.5 ND filter and an acquisition time of 15 s.

$$\text{Disp}(G) = \left| \frac{\text{Pos}(G)_{633 \text{ nm}} - \text{Pos}(G)_{532 \text{ nm}}}{\lambda_{633 \text{ nm}} - \lambda_{532 \text{ nm}}} \right| \quad (1)$$

Raman spectra were acquired from 30 individual nanowires across multiple independently synthesized 3DFG-Si NW samples ($n = 3$) per synthesis condition.

Lattice Thermal Conductivity of the Si Nanowire and Graphene Based on DFT. The lattice thermal conductivity was

calculated by solving the linearized Peierls–Boltzmann transport equation iteratively. The second-order and third-order interatomic force constants (IFCs) were extracted from DFT calculations using the projector-augmented wave method²⁷ in the Vienna *ab initio* simulation package (VASP).²⁸ The local density approximation (LDA) was used for the exchange–correlation functional.²⁹ The self-consistent calculation was conducted with a 500 eV cutoff energy for Si and 600 eV for graphene and a force convergence criterion of 10^{−6} eV/Å for both materials. Supercells of 4 × 4 × 4 and 5 × 5 × 1 were used for Si and graphene, respectively. For Si, the phonon relaxation time was calculated by including phonon–phonon, phonon–isotope, and phonon–boundary scattering terms based on the Matthiessen rule. The phonon–phonon scattering rates were determined using third-order IFCs from DFT with a 4 × 4 × 4 supercell. The isotopes are assumed to be a naturally occurring case. The linearized Peierls–Boltzmann transport equation was solved to obtain the lattice thermal conductivity with a 28 × 28 × 28 sampling grid for phonon states using an iterative manner as implemented in Boltzmann transport equation (BTE).³⁰ More technical details can be found in previous publications.^{30–34} For graphene, the lattice thermal conductivity was calculated under the ballistic limit, assuming a mean free path of 20 nm. The sampling grid for phonon states is 41 × 41 × 1.

Thermal Conductance of Graphene–Graphene Junctions Based on MD Simulations. We calculated the thermal conductance of graphene–graphene junctions (monolayer–monolayer, bilayer–bilayer, and trilayer–trilayer) using non-equilibrium molecular dynamics (NEMD) simulations implemented in LAMMPS.³⁵ The simulation was performed using the AIREBO-Morse potential,³⁶ with a time step of 1 fs. Boundary conditions were fixed along the heat flow direction and periodic along both perpendicular directions, with a vacuum of 15 Å along the cross-plane direction applied to avoid interactions between two adjacent images. The system was first equilibrated within the NVT (constant number of particles N , volume V , and temperature T) ensemble with a Nose–Hoover thermostat for 300 ps and then in the NVE (constant energy E) ensemble for 100 ps. After that, a heat current was enabled by contacting the two ends (with a thickness of 21 Å) of the simulation domain with the hot and cold reservoirs using the Langevin thermostats. The temperatures of the hot and cold reservoirs were set as $T_H = T_0 + 0.2T_0$ and $T_C = T_0 - 0.2T_0$, respectively, where T_0 is the mean temperature of the system. We used 2 ns to stabilize the temperature gradient and the next 2 ns to average the temperature profile, which was then used to calculate the junction conductance. Since the considered temperatures are lower than the Debye temperature, we applied quantum corrections to the temperature using the semiclassical definition:^{37,38}

$$3(N - 1)k_B T_{\text{MD}} = \sum_{\lambda} \hbar \omega_{\lambda} \left[\frac{1}{2} + \frac{1}{\exp(\hbar \omega_{\lambda} / k_B T_{\text{real}}) - 1} \right] \quad (2)$$

where k_B is the Boltzmann constant, \hbar is Planck's constant, ω_{λ} is the frequency of the phonon mode λ , and T_{real} and T_{MD} represent the real temperature and the corresponding temperature in MD simulation, respectively.

ASSOCIATED CONTENT

Supporting Information

The Supporting Information is available free of charge at <https://pubs.acs.org/doi/10.1021/acsami.1c08093>.

Brief descriptions of Raman spectroscopy, thermal contact resistance measurement, thermal conductivity of intrinsic Si nanowires, FTIR spectra of 3DFG-Si NWs, uncertainty calculation of thermal conductivity measurement, lattice thermal conductivity of the Si nanowire and graphene, and thermal conductance of graphene–graphene junctions (PDF)

AUTHOR INFORMATION

Corresponding Authors

Sangyeop Lee – Department of Mechanical Engineering and Materials Science, University of Pittsburgh, Pittsburgh, Pennsylvania 15261, United States; Email: sylee@pitt.edu

Tzahi Cohen-Karni – Department of Materials Science Engineering and Department of Biomedical Engineering, Carnegie Mellon University, Pittsburgh, Pennsylvania 15213, United States; Email: tzahi@andrew.cmu.edu

Sheng Shen – Department of Mechanical Engineering, Carnegie Mellon University, Pittsburgh, Pennsylvania 15213, United States; orcid.org/0000-0002-9951-0814; Email: sshen1@cmu.edu

Authors

Wei Gong – Department of Mechanical Engineering, Carnegie Mellon University, Pittsburgh, Pennsylvania 15213, United States

Raghav Garg – Department of Materials Science Engineering, Carnegie Mellon University, Pittsburgh, Pennsylvania 15213, United States; orcid.org/0000-0002-3501-6892

Ruiqiang Guo – Department of Mechanical Engineering and Materials Science, University of Pittsburgh, Pittsburgh, Pennsylvania 15261, United States

Complete contact information is available at: <https://pubs.acs.org/10.1021/acsami.1c08093>

Author Contributions

[†]W. Gong, R. Garg, and R. Guo contributed equally to this work.

Notes

The authors declare no competing financial interest. The data that support the findings of this study are available from the corresponding authors upon reasonable request.

ACKNOWLEDGMENTS

This work was primarily supported by the National Science Foundation under awards CMMI-1334630 and CMMI-1916110 for sample preparation, thermal measurements, and data analysis. The authors acknowledge Mr. Xiao Luo for useful discussion and the assistance on manuscript preparation. R. Garg and T.C.-K. acknowledge funding support from the National Science Foundation under award CBET-1552833, the Defense Advanced Research Projects Agency under award AWD00001593 (416052-5), and the National Institute of Health under award R21EB029164. R. Guo and S.L. acknowledge the support from National Science Foundation under award CBET-1943807. The simulation was performed using the computational resources of the Center for Research Computing at the University of Pittsburgh. R. Garg and T.C.-K. acknowledge the support from the Department of Materials Science and Engineering Materials Characterization Facility at Carnegie Mellon University supported by grant MCF-677785.

REFERENCES

- (1) Novoselov, K. S.; Geim, A. K.; Morozov, S. V.; Jiang, D.; Zhang, Y.; Dubonos, S. V.; Grigorieva, I. V.; Firsov, A. A. Electric Field in Atomically Thin Carbon Films. *Science* **2004**, *306*, 666–669.
- (2) Lui, C. H.; Liu, L.; Mak, K. F.; Flynn, G. W.; Heinz, T. F. Ultraflat Graphene. *Nature* **2009**, *462*, 339–341.
- (3) Geim, A. K. Graphene: Status and Prospects. *Science* **2009**, *324*, 1530–1534.

(4) Choi, W.; Lahiri, I.; Seelaboyina, R.; Kang, Y. S. Synthesis of Graphene and Its Applications: A Review. *Crit. Rev. Solid State Mater. Sci.* **2010**, *35*, 52–71.

(5) Zhang, Y.; Zhang, L.; Zhou, C. Review of Chemical Vapor Deposition of Graphene and Related Applications. *Acc. Chem. Res.* **2013**, *46*, 2329–2339.

(6) Geim, A. K.; Novoselov, K. S. The Rise of Graphene. *Nat. Mater.* **2007**, *6*, 183–191.

(7) Balandin, A. A.; Ghosh, S.; Bao, W.; Calizo, I.; Teweldebrhan, D.; Miao, F.; Lau, C. N. Superior Thermal Conductivity of Single-Layer Graphene. *Nano Lett.* **2008**, *8*, 902–907.

(8) Ghosh, S.; Calizo, I.; Teweldebrhan, D.; Pokatilov, E. P.; Nika, D. L.; Balandin, A. A.; Bao, W.; Miao, F.; Lau, C. N. Extremely High Thermal Conductivity of Graphene: Prospects for Thermal Management Applications in Nanoelectronic Circuits. *Appl. Phys. Lett.* **2008**, *92*, 151911.

(9) Garg, R.; Rastogi, S. K.; Lamparski, M.; de la Barrera, S. C.; Pace, G. T.; Nuhfer, N. T.; Hunt, B. M.; Meunier, V.; Cohen-Karni, T. Nanowire-Mesh-Templated Growth of Out-of-Plane Three-Dimensional Fuzzy Graphene. *ACS Nano* **2017**, *11*, 6301–6311.

(10) Garg, R.; Gopalan, D. P.; de la Barrera, S. C.; Hafiz, H.; Nuhfer, N. T.; Viswanathan, V.; Hunt, B. M.; Cohen-Karni, T. Electron Transport in Multidimensional Fuzzy Graphene Nanostructures. *Nano Lett.* **2019**, *19*, 5335–5339.

(11) Cohen-Karni, T.; Timko, B. P.; Weiss, L. E.; Lieber, C. M. Flexible Electrical Recording from Cells Using Nanowire Transistor Arrays. *Proc. Natl. Acad. Sci. U. S. A.* **2009**, *106*, 7309–7313.

(12) San Roman, D.; Krishnamurthy, D.; Garg, R.; Hafiz, H.; Lamparski, M.; Nuhfer, N. T.; Meunier, V.; Viswanathan, V.; Cohen-Karni, T. Engineering Three-Dimensional (3D) Out-of-Plane Graphene Edge Sites for Highly Selective Two-Electron Oxygen Reduction Electrocatalysis. *ACS Catal.* **2020**, *10*, 1993–2008.

(13) Garg, R.; Roman, D. S.; Cohen-Karni, T. Multidimensional Graphene Nanostructures – Synthesis and Applications. *Pure Appl. Chem.* **2020**, *92*, 1929–1936.

(14) Dato, A.; Radmilovic, V.; Lee, Z.; Phillips, J.; Frenklach, M. Substrate-Free Gas-Phase Synthesis of Graphene Sheets. *Nano Lett.* **2008**, *8*, 2012–2016.

(15) Suenaga, K.; Sandré, E.; Colliex, C.; Pickard, C. J.; Kataura, H.; Iijima, S. Electron Energy-Loss Spectroscopy of Electron States in Isolated Carbon Nanostructures. *Phys. Rev. B* **2001**, *63*, 165408.

(16) Dato, A.; Frenklach, M. Substrate-Free Microwave Synthesis of Graphene: Experimental Conditions and Hydrocarbon Precursors. *New J. Phys.* **2010**, *12*, 125013.

(17) Jorissen, K.; Rehr, J. J.; Verbeeck, J. Multiple Scattering Calculations of Relativistic Electron Energy Loss Spectra. *Phys. Rev. B* **2010**, *81*, 155108.

(18) Gass, M. H.; Bangert, U.; Bleloch, A. L.; Wang, P.; Nair, R. R.; Geim, A. K. Free-Standing Graphene at Atomic Resolution. *Nat. Nanotechnol.* **2008**, *3*, 676–681.

(19) Huang, J. Y. HRTEM and EELS Studies of Defects Structure and Amorphous-like Graphite Induced by Ball-Milling. *Acta Mater.* **1999**, *47*, 1801–1808.

(20) Shi, L.; Li, D.; Yu, C.; Jang, W.; Kim, D.; Yao, Z.; Kim, P.; Majumdar, A. Measuring Thermal and Thermoelectric Properties of One-Dimensional Nanostructures Using a Microfabricated Device. *J. Heat Transfer* **2003**, *125*, 881–888.

(21) Li, D.; Wu, Y.; Kim, P.; Shi, L.; Yang, P.; Majumdar, A. Thermal Conductivity of Individual Silicon Nanowires. *Appl. Phys. Lett.* **2003**, *83*, 2934–2936.

(22) Yin, L.; Kyung Lee, E.; Woon Lee, J.; Whang, D.; Lyong Choi, B.; Yu, C. The Influence of Phonon Scatterings on the Thermal Conductivity of SiGe Nanowires. *Appl. Phys. Lett.* **2012**, *101*, No. 043114.

(23) Balachander, N.; Seshadri, I.; Mehta, R. J.; Schadler, L. S.; Borca-Tasciuc, T.; Keblinski, P.; Ramanath, G. Nanowire-Filled Polymer Composites with Ultrahigh Thermal Conductivity. *Appl. Phys. Lett.* **2013**, *102*, No. 093117.

- (24) Persson, A. I.; Koh, Y. K.; Cahill, D. G.; Samuelson, L.; Linke, H. Thermal Conductance of InAs Nanowire Composites. *Nano Lett.* **2009**, *9*, 4484–4488.
- (25) Pettes, M. T.; Ji, H.; Ruoff, R. S.; Shi, L. Thermal Transport in Three-Dimensional Foam Architectures of Few-Layer Graphene and Ultrathin Graphite. *Nano Lett.* **2012**, *12*, 2959–2964.
- (26) Hasan, M. A.; Sangashetty, R.; Esther, A. C. M.; Patil, S. B.; Sherikar, B. N.; Dey, A. Prospect of Thermal Insulation by Silica Aerogel: A Brief Review. *J. Inst. Eng. (India): Ser. D* **2017**, *98*, 297–304.
- (27) Blöchl, P. E. Projector Augmented-Wave Method. *Phys. Rev. B* **1994**, *50*, 17953–17979.
- (28) Kresse, G.; Furthmüller, J. Efficient Iterative Schemes for Ab Initio Total-Energy Calculations Using a Plane-Wave Basis Set. *Phys. Rev. B* **1996**, *54*, 11169–11186.
- (29) Perdew, J. P.; Burke, K.; Ernzerhof, M. Generalized Gradient Approximation Made Simple. *Phys. Rev. Lett.* **1996**, *77*, 3865–3868.
- (30) Li, W.; Carrete, J.; Katcho, N. A.; Mingo, N. ShengBTE: A Solver of the Boltzmann Transport Equation for Phonons. *Comput. Phys. Commun.* **2014**, *185*, 1747–1758.
- (31) Guo, R.; Wang, X.; Huang, B. Thermal Conductivity of Skutterudite CoSb₃ from First Principles: Substitution and Nano-engineering Effects. *Sci. Rep.* **2015**, *5*, 7806.
- (32) Lindsay, L.; Broido, D. A.; Reinecke, T. L. Thermal Conductivity and Large Isotope Effect in GaN from First Principles. *Phys. Rev. Lett.* **2012**, *109*, No. 095901.
- (33) Ward, A.; Broido, D. A.; Stewart, D. A.; Deinzer, G. Ab Initio Theory of the Lattice Thermal Conductivity in Diamond. *Phys. Rev. B* **2009**, *80*, 125203.
- (34) Broido, D. A.; Malorny, M.; Birner, G.; Mingo, N.; Stewart, D. A. Intrinsic Lattice Thermal Conductivity of Semiconductors from First Principles. *Appl. Phys. Lett.* **2007**, *91*, 231922.
- (35) Plimpton, S. Fast Parallel Algorithms for Short-Range Molecular Dynamics. *J. Comput. Phys.* **1995**, *117*, 1–19.
- (36) O'Connor, T. C.; Andzelm, J.; Robbins, M. O. AIREBO-M: A Reactive Model for Hydrocarbons at Extreme Pressures. *J. Chem. Phys.* **2015**, *142*, No. 024903.
- (37) Turney, J. E.; McGaughey, A. J. H.; Amon, C. H. Assessing the Applicability of Quantum Corrections to Classical Thermal Conductivity Predictions. *Phys. Rev. B* **2009**, *79*, 224305.
- (38) Bedoya-Martínez, O. N.; Barrat, J.-L.; Rodney, D. Computation of the Thermal Conductivity Using Methods Based on Classical and Quantum Molecular Dynamics. *Phys. Rev. B* **2014**, *89*, No. 014303.